Graduate School of Frontier Sciences, The University of Tokyo

Department of Socio-Cultural Environmental Studies

2021

Master's Thesis

Spatiotemporal Variation of Sea Surface Temperature Based on Landsat-8 in Tokyo Bay

Landsat-8 データによる東京湾海面水温の時空間変化

Submitted on July 9, 2021

Advisor: Professor Jun SASAKI

Xu Rui

徐　鋭

Table of Contents

List of Figures

List of Tables

1 Introduction

1.1 Background

1.1.1 Importance of Measuring Sea Surface Temperature

Sea surface temperature (SST) is the water temperature close to the ocean's surface, which represents the temperature measured between 1 millimetre (0.04 in) and 20 metres (70 ft) below the sea surface [1]. SST is a fundamental physical variable for understanding, quantifying and predicting complex interactions between the ocean and the atmosphere, which directly impact large- and small-scale weather and climate patterns. Monitoring and Mapping SST has been considered necessary and meaningful in case of oceanic issues.

Sea surface temperature not only indicates the global climate change but also reveals productivity of harvesting closely related to anthropogenic activities. It has been proved that SST plays an important role in responses of the seagrass meadows. Japan has a wide range of climate zones from cold temperate to subtropical, reflecting its wide geographical extent from north to south, as well as the influence of two major warm and cold currents, the Kuroshio and Oyashio, respectively [2]. Seaweed beds are communities consisting of large benthic plants and distributed widely along Japanese coasts, which are mainly classified into three groups, a seagrass bed, a kelp forest and a Sargassum bed [3]. Species constituting seaweed beds in Japan vary depending on localities due to the influence of cold and warm currents. In Japan, cultivation, as well as harvesting, from natural populations, has sustained the Japanese seaweed industry for many years, which is widely practiced in many coastal areas around the archipelago. But recently a down-fall in seaweed production and seagrass meadows have been experienced in some areas

for certain species due to warming oceans [3]. Many factors have been proposed that could lead to an increase in seawater temperature around coastal areas, including thermal discharge from power plants.

1.1.2 Thermal Discharge from Power Plants

In thermal or nuclear power plants, electricity is generated by rotating turbines with high-temperature steam. After use, the steam is sent to a condenser where it is cooled back to water and used again in the boiler or nuclear reactor (steam generator). Because Japanese power plants are located near the coast, the condenser is seawater-cooled, and the seawater used to cool the steam in the condenser is discharged directly into the ocean as warm wastewater. Excess heat discharged as cooling water from coastal thermal power plants is an important form of regional anthropogenic heat [4]. Most previous studies have shown that thermal discharge can increase seawater temperature, which directly affects the environmental temperature of marine organisms, like the number and community structure of phytoplankton, zooplankton, macrobenthos, and swimming animals as well as their habitats [5]. With the diffusion of thermal discharge in the water, the temperature of the receiving water within a certain area near power plants will have a 1-3 degree increase at the surface layer, as shown in Fig. 1.1 [6]. The thermal discharge on aquatic ecosystems has become an important issue in the field of marine and environmental protection.

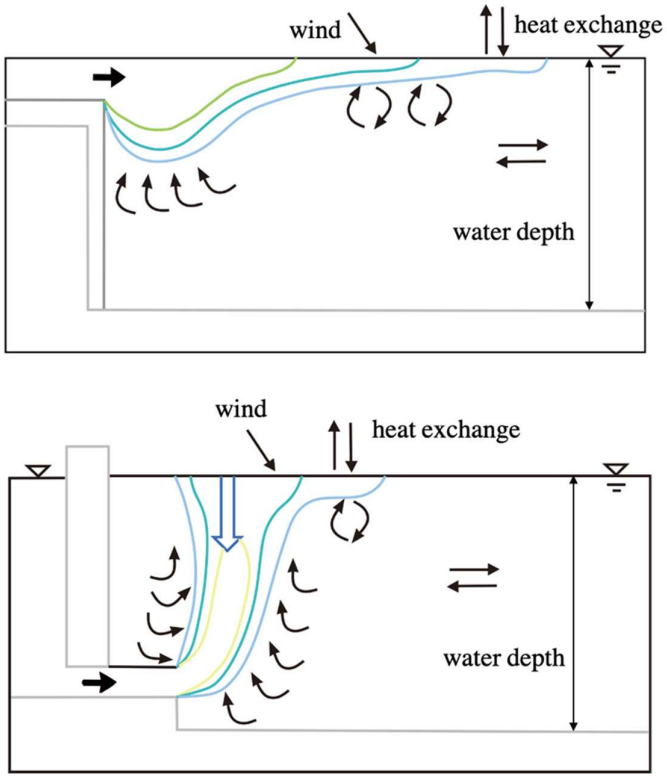

Fig. 1.1 Power plant drainage diffusion diagram [6]

Although the diffusion diagram indicates the effects of the thermal discharge of power plants on surrounding sea surface temperature based on many simulation results, the actual situation must be more considerably complicated caused by various factors like sea currents, water exchange and tide. Therefore, it is very important to understand how the thermal discharge of power plants affects the surrounding seawater temperature in real situations.

1.1.3 Identification of the Impacts of Thermal Discharge

The increasing amount of power produced by fossil fuel and nuclear power plants makes it important to monitor the thermal pollution in coastal waters. Much of the research on

this problem has focused on the assessment of the impact on marine biological communities. It is fundamental to detect the intensity of heated effluent discharge and its spatial and temporal properties [7].

The conventional method for investigation of this kind of thermal pollution is to measure the water temperature from point to point, a major expense in time and money. With in-situ measurements, it is hard to get accurate distributions of the thermal discharge because of tides and advection.

In recent years, satellite-based sensors like Landsat and Sentinel have been successfully used to estimate and visualize the distribution of coastal sea surface temperature due to their wide coverage and high radiometric resolution due to their ability to measure the temperature of the top millimeter of the ocean surface. Since the launch of Landsat 8, high-quality sea surface observation data have been acquired, which makes it essential to study the highly variable small-scale oceanic phenomena in a coastal region. But the corresponding sea surface temperature products have not been collected, sea surface temperature images still need to be obtained based on retrieval algorithms.

1.2 Literature Review

1.2.1 Temperature Retrieval Methods

In order to obtain accurate temperature data, a few studies have discussed various inversion algorithms to transform original satellite data to Land Surface Temperature (LST) or SST data. Radiative transfer equation (RTE) was the first algorithm used [10]. The next algorithm called mono-window algorithm was developed by Qin et al (2001) [11] and single-channel by Jiminez-Munoz and Sobrino (2003) [15]. Many algorithms in recent years have been improved based on the initial mono-window algorithm.

Furthermore, split windows [12], and multi-angle algorithms [13] were the advanced methods used. The method which is mostly used by many researchers is the NASA methodology contained in the Landsat science data user handbook in each series of Landsat [14]. The value of land surface temperature starts from the conversion of the digital number (DN) to spectral radiance and then obtains the brightness temperature (K) [15].

With the increasing volume of data processing and the need for high efficiency, corresponding method has been created. Sofia L. Ermida et al [16] developed a code repository that allowed computing LSTs from satellite Landsat 4 to Landsat 8, making use of the computational resources of Google's servers. In their study, LST was converted with the mono-window algorithm improved and used by the Satellite Application Facility on Climate Monitoring from European Organization for the Exploitation of Meteorological Satellites (EUMETSAT). Compared to previous methods, uses were not required to download the data from official websites. The retrieval process and analysis could be performed within a Google online platform simply by accessing the code. It mentioned that the code repository developed was for LST retrieval and the code should be edited to better meet different needs. This leaves room for improvement of utilizing computational resources and online platform to satisfy the demand for SST retrieval and efficient and accurate output methods.

1.2.2 Analysis of Thermal Discharge on SST

In terms of SST on small-scale areas affected by industrial activities, some previous studies have tried to analyze industrial thermal plumes. Shih-Jen Huang [17] applied the algorithm to estimate the SST from the thermal band of Landsat 7 ETM+, and then it analyzed the impact of the tide on the thermal plume. Jie Lin [18] quantitatively estimated

the correlation between SST increment and install capacity of thermal plants through in-site survey and Modis satellite. They showed the potential of analyzing the effects of thermal discharge on SST using satellite images, however, the resolution of satellites used in these studies was not high enough and there were no spatial variation results in seasonal scale.

1.3 Objectives

A few studies have proposed Land Surface Temperature (LST) or Sea Surface Temperature (SST) retrieval algorithms for the satellite data. While most algorithms are simple to implement, they require users to provide the necessary input data and calibration coefficients, which are generally not readily available. Since the data are only accessible through the web application, common methods still require users to download large amounts of data if they wish to perform time-series analysis.

Google Earth Engine (GEE) is an online platform created to allow remote sensing users to easily perform big data analysis without increasing the demand for local computing resources and create image results quickly. Whether you want to get processed results for any day, any month, or any year at the same time, GEE can do it all. Another advantage of GEE is that by modifying the code directly you can get the results of various calculations shown on the platform such as time series analysis while completing the temperature inversion from satellite original data.

As mentioned by Sofia L. Ermida et al [16], a relatively new approach has been developed to derive Landsat LST based on GEE. Unfortunately, the code cannot be directly utilized for SST retrieval. Furthermore, modifications are still required under some circumstances for SST mapping efficiently.

Hence, this study aims to make clear the spatiotemporal variation of SST based on satellite data. To be more specific, first, modify and develop the code to make it more applicable in efficient SST mapping. Second, visualize and identify the SST distribution patterns in the study site especially in coastal zones that are easily affected by thermal power plants through GEE.

1.4 Significance and Originality

As people continue to pay attention to the impact of water temperature changes on the water environment, efficient temperature monitoring and analysis continue to become increasingly important.

Before this study, the latest approach on using GEE to acquire temperature data is applicable to LST [16]. By improving the code, the edited method can be widely used for acquiring high-resolution SST images through Landsat. In addition, this study also aims to provide a basis for resolving stresses of coastal zone environment issues in space and time and support sustainable coastal zone management by discussing thermal discharges and seagrass meadows.

2 Materials and Methods

2.1 Study Site Description

2.1.1 Tokyo Bay

Tokyo Bay (Fig. 2.1) is located in the southern Kantō region of Japan, 80 km long trending north to south. The bay is separated into inner and outer areas by a 7 km-wide strait between Cape Futtsu and Cape Kannon. From Cape Futtsu to Cape Suzaki, and from Kannonzaki to Kenzaki, there are many sandy beaches, seagrass and seaweed beds that are significant to organisms as habitats. Large-scale tidal flats such as Banshu Tidal Flat and Futtsu Tidal Flat are scattered from Kisarazu to Futtsu.

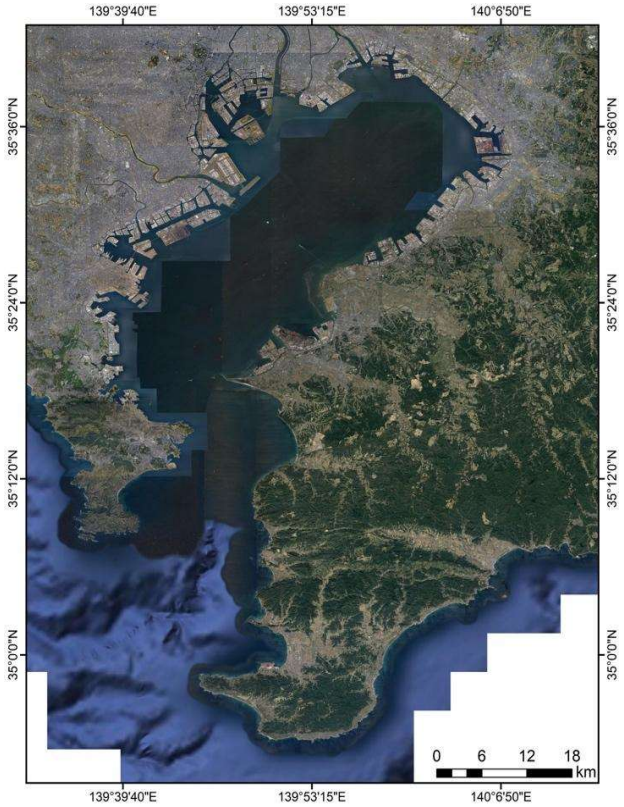

Fig. 2.1 Study site location (source: google map)

The study site is also chosen according to large amounts of thermal power plants. Most of the thermal power plants owned by Tokyo Electric Power Company (TEPCO) which is the largest electric utility in Japan and the 4th largest electric utility in the world are located along the coast of Tokyo Bay (Fig. 2.2). Among these power plants, the Futtsu Power Station is the fourth largest gas-fired power station in the world, situated on the north of Futtsu Cape which faces Tokyo Bay, with power operation at 5,040 MW [19]. Driven by the seawater-cooling system in thermal power plants, great quantities of cooling water are discharged into Tokyo Bay, directly affecting seawater temperature. To conclude, Tokyo Bay is chosen as a study site since it is representative and meaningful for its large-scale seagrass and seaweed beds and concentrated thermal power plants regarding the study target. The impact of thermal discharge on the aquatic environment of Tokyo Bay is expected to be significant. Furthermore, sufficient real-time data provided by monitoring stations in Tokyo Bay is significant and necessary for verification work.

Fig. 2.2 Power plants around Tokyo Bay (source: google map)

2.1.2 Futtsu Tidal Flat in Tokyo Bay

A sandy tidal flat spreading on the northeast side of Cape Futtsu, a cape located east of Tokyo Bay (Fig. 2.3). There are seaweed beds of eelgrass, and the eastern part is a tidal flat. Futtsu tidal flat has the largest remaining eelgrass bed in Tokyo Bay.

Fig. 2.3 Futtsu tidal flat (source: google map)

Analysis of long-term variation in the area of eelgrass beds from the 1960s to the present reveals that the total area of eelgrass beds fluctuated significantly from a maximum of 1.28 km^2(1987) to a minimum of 0.39 km^2 (2001) [20].

2.1.3 Wajiro Tidal Flat in Hakata Bay

Wajiro Tidal Flat is a tidal flat of about 80 hectares in the area located at the northeastern end of Hakata Bay (Fig. 2.4).

Fig. 2.4 Hakata Bay and Wajiro tidal flat (red circle) (source: google map)

2.2 Google Earth Engine Code Editor

The Earth Engine Code Editor is an interactive environment for developing complex geospatial workflows fast and easily. In general, the whole workbench can be divided into four major parts: script file storage area, code editing area, output console and result map display area, shown as Fig. 2.5. By running the code editor, the scripts developed in the editing area are sent to Google for processing and the generated map tiles and messages are sent back for display in the Map and Console tab.

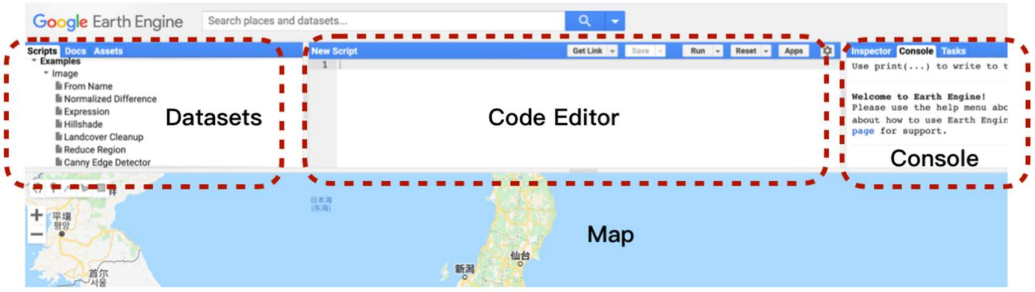

Fig. 2.5 Diagram of components of the Earth Engine Code Editor

2.3 Data

The Landsat 8 Operational Land Imager and Thermal Infrared Sensor (OLI/TIRS) makes it possible to obtain high-resolution SST images of coastal regions. Compared with other available satellite products, Landsat 8 has the most important strength with the highest resolution of 100m in its two thermal bands. A comparison is shown in Table. 2.1.

Table. 2.1 Comparison among Landsat 8, Modis and Sentinel-3 [21]

Name	Revisit frequency(day)	Resolution	Data range
Landsat 8	16 days	100 m	2013-present
Modis	1-2 days	1000 m	2002-present
Sentinel-3	1 day	500 m	2016-present

Landsat 8 has a 16-day repeat cycle, relatively longer than other satellites such as Modis and Sentinel-3, of which the repeat cycle is 1-2 days and 1 day respectively. However, the study focuses on the coastal area, in which case, the spatial resolution should be the first consideration to monitor the small-scale features of estuaries and coastal regions. The feasibility of temporal trending analysis will be discussed in the study with the limitation of Landsat 8 datasets from 2013 to 2020.

The Thermal Infrared Sensor (TIRS) owned by Landsat 8 contains two thermal bands, band 10 and band 11, centered at 11 and 12 μm that measure Earth's thermal energy. Both bands from TIRS are long wavelengths. Landsat 8 orbits the Earth in a sun-synchronous, near-polar orbit, at an altitude of 705 km (438 mi), inclined at 98.2 degrees, and completes one Earth orbit every 99 minutes [21]. The satellite cycles with an equatorial crossing time: 10:00 a.m. +/- 15 minutes. A detailed overview of Landsat 8 and its thermal infrared sensor is given in Table. 2.2.

Table. 2.2 Landsat 8 bands information [21]

Spectral Band	Wavelength	Resolution	Solar Irradiance
Band 1 - Coastal / Aerosol	0.433 – 0.453 µm	30 m	2031 W/(m^{2}µm)
Band 2 - Blue	0.450 – 0.515 µm	30 m	1925 W/(m^{2}µm)
Band 3 - Green	0.525 – 0.600 µm	30 m	1826 W/(m^{2}µm)
Band 4 - Red	0.630 – 0.680 µm	30 m	1574 W/(m^{2}µm)
Band 5 - Near Infrared	0.845 – 0.885 µm	30 m	955 W/(m^{2}µm)
Band 6 - Short Wavelength Infrared	1.560 – 1.660 µm	30 m	242 W/(m^{2}µm)
Band 7 - Short Wavelength Infrared	2.100 – 2.300 µm	30 m	82.5 W/(m^{2}µm)
Band 8 - Panchromatic	0.500 – 0.680 µm	15 m	1739 W/(m^{2}µm)
Band 9 - Cirrus	1.360 – 1.390 µm	30 m	361 W/(m^{2}µm)
Band 10 - Long Wavelength Infrared	10.30 – 11.30 µm	100m	
Band 11 - Long Wavelength Infrared	11.50 – 12.50 µm	100m	

2.3.1 Landsat 8 Data

Initially, all multispectral Landsat 8 image data is represented by quantized and calibrated scaled Digital Numbers (DN), which is delivered in 16-bit unsigned integer format with a range from 0 and 65536. As has been summarized by the United States Geological Survey (USGS), Landsat Collections Level-1 data can be rescaled to top of atmosphere (TOA) reflectance and radiance using radiometric rescaling coefficients provided in the metadata file that is delivered with the Level-1 product. The thermal band data can be converted to TOA brightness temperature with the metadata file. First, in order to start with radiometric calibration, TOA radiance can be required as [22]:

$$L_\lambda = M_L Q_{cal} + A_L \tag{2.1}$$

where:

L_λ =TOA spectral radiance (Watts / (m^2 * srad * μm))

M_L =Band-specific multiplicative rescaling factor from the metadata (RADIANCE_MULT_BAND_x, where x is the band number)

A_L =Band-specific additive rescaling factor from the metadata

(RADIANCE_ADD_BAND_x, where x is the band number)

Q_{cal} = Quantized and calibrated standard product pixel values (DN)

Meanwhile, reflective band DN's can be converted to TOA reflectance:

$$\rho'_\lambda = M_\rho Q_{cal} + A_\rho \quad (2.2)$$

where:

ρ'_λ = TOA planetary reflectance, without correction for solar angle. Note that ρλ' does not contain a correction for the sun angle.

M_ρ =Band-specific multiplicative rescaling factor from the metadata (REFLECTANCE_MULT_BAND_x, where x is the band number)

A_ρ =Band-specific additive rescaling factor from the metadata (REFLECTANCE_ADD_BAND_x, where x is the band number)

Q_{cal} = Quantized and calibrated standard product pixel values (DN)

Following the calibration of TOA radiance, thermal band data can be converted to TOA brightness temperature as:

$$T = \frac{K_2}{ln\left(\frac{K_1}{L_\lambda}+1\right)} \quad (2.3)$$

where:

T = Top of atmosphere brightness temperature (K)

L_λ = TOA spectral radiance (Watts / (m2 * srad * μm))

K1 =Band-specific thermal conversion constant from the metadata (K1_CONSTANT_BAND_x, where x is the thermal band number)

K2 =Band-specific thermal conversion constant from the metadata (K2_CONSTANT_BAND_x, where x is the thermal band number)

In the method proposed by Sofia L. Ermida et al [16], TOA brightness temperatures are fully available and ready to use in GEE. The data from the Landsat series are considered consistent and inter-calibrated, and all TIR bands have been resampled to 30 m spatial resolution. Besides the TIR band, the red and near-infrared (NIR) bands are used to derive the Normalized Difference Vegetation Index (NDVI), which is calculated from the surface reflectance (SR) values. The SR data are also available in GEE, provided by the USGS. Moreover, Cloud coverage information, including cloud shadowing, can be retrieved from the quality assessment band (BQA), which is also made available by the USGS through GEE.

2.3.2 Atmospheric Data

Atmospheric water vapor (WV) is required for the accurate retrieval of the surface temperature from remote sensing data and other applications. Total Column Water Vapor (TCWV) values from the National Center for Environmental Prediction (NCEP) and National Center for Atmospheric Research (NCAR) reanalysis data are available on GEE [23]. The TCWV data are available globally from 1948 to the present. The data are linearly interpolated to each Landsat image acquisition time, with a six-hourly temporal resolution and 2.5 degrees spatial resolution.

2.3.3 Surface Emissivity

The surface emissivity can be derived from the Advanced Spaceborne Thermal Emission and Reflection Radiometer Global Emissivity Database (ASTER GED) developed by the

National Aeronautics and Space Administration's (NASA) Jet Propulsion Laboratory (JPL), as directly provided by GEE, corresponding to the average of all retrievals performed over an eight-year period [24]. However, the emissivity varies over time due to variations in vegetation density. A vegetation adjustment using Landsat derived NDVI and mean ASTER GED NDVI has been applied to derive the fraction of vegetation cover (FVC), shown as:

$$FVC = \left(\frac{NDVI - NDVI_{bare}}{NDVI_{veg} - NDVI_{bare}}\right)^2 \quad (2.4)$$

where $NDVI_{bare}$ and $NDVI_{veg}$ are the NDVI values of completely bare and fully vegetated pixels, respectively. Following previous studies [25], these two threshold values are set to $NDVI_{bare}$= 0.2 and $NDVI_{veg}$ = 0.86.

Pixels with NDVI below $NDVI_{bare}$ are considered completely bare, while pixels with NDVI above $NDVI_{veg}$ are considered fully vegetated.

The calculation of Emissivity values can follow using the Vegetation-Cover method, which is defined as:

$$\varepsilon_b = FVC\varepsilon_b + (1 - FVC)\varepsilon_{b,bare} \quad (2.5)$$

Where $\varepsilon_{b,veg}$ and $\varepsilon_{b,bare}$ are the emissivity of vegetation and bare ground for a given spectral band b which are derived from the original ASTER emissivity. The emissivity of vegetated surfaces typically shows relatively small variations in the TIR region.

2.3.4 Land Area Masking Dataset

Land area was masked according to the surface water dataset provided by GEE called

'JRC Monthly Water Recurrence'. The dataset contains maps of the location and temporal distribution of surface water from 1984 to 2020. Each pixel was individually classified into water / non-water. Compared with coastline polygon data, the dataset provides dynamic images which are more accurate for temporal analysis since the water area is always changing. To avoid unnecessary computation time, the land area was masked out and the target water area was extracted, as shown in Fig. 2.6. The coastline of results presented by GEE will also be fixed again in ArcGIS based on the data provided by ArcGIS Japan and Geospatial Information Authority of Japan [26] to improve the reliability of coastlines.

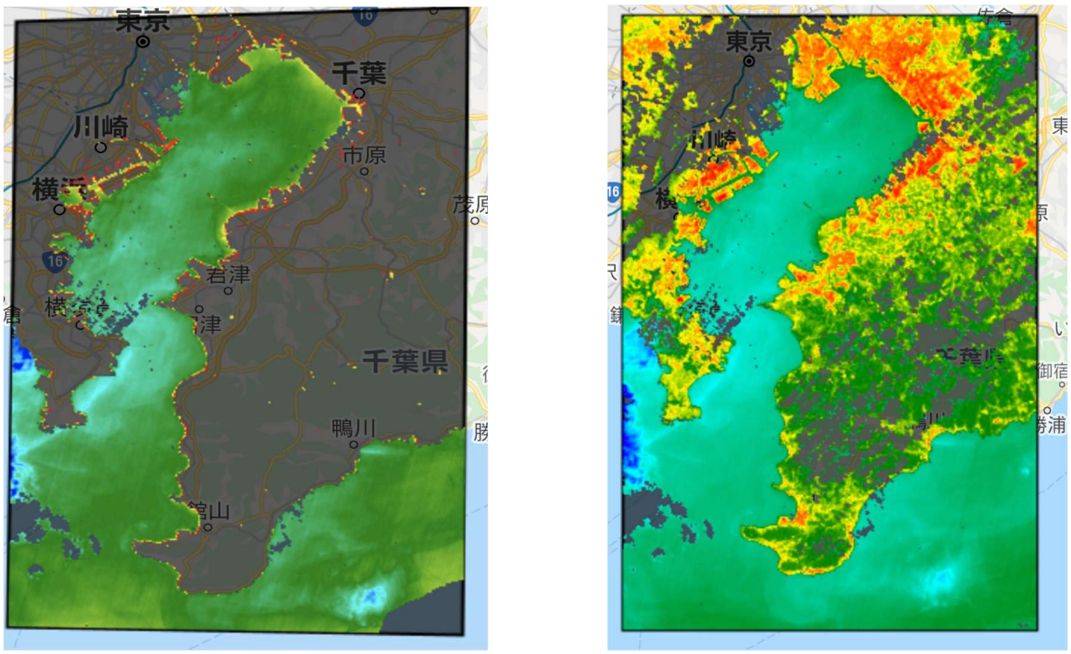

Fig. 2.6 Result with a mask (left) on GEE map

Result without a mask (right) on GEE map

2.3.5 Monitoring Station Data

The monitoring data is provided from 2013 to 2020 by several monitoring stations scattered in Tokyo Bay. The dataset is suitable for verifying the accuracy of satellite data since it is hourly data, which can be directly acquired from Tokyo Bay Environmental Information Center [27]. Basically, the satellite cycles with an equatorial crossing time: from 10:15 a.m. to 10:16 a.m., each monitoring data was matched with the nearest Landsat SST within a temporal and spatial window of 1 hour and 1 km centered at the monitoring location.

2.4 Methods

2.4.1 SST Retrieval Algorithm

High spatial resolution LST datasets are currently not available in GEE, consequently, LSTs or SSTs need to be computed through retrieval process. When it comes to SST retrieval, mono window algorithm (MW) and split-window algorithm (SW) are widely applied, using one thermal band and two thermal bands respectively [12,13]. However, the USGS pointed out that, given the larger uncertainty in the Band 11 values, users should work with TIRS Band 10 data as a single spectral band. Band 10 also has higher accuracy atmospheric transmittance values.

In this case, SST is computed with the Statistical Mono Window algorithm (SMW). The algorithm used in this study was developed by the Satellite Application Facility on Climate Monitoring which has been proved to be suitable for the GEE platform [16]. It was used for LST retrieval initially, while the approach is based on an empirical relationship between TOA brightness temperatures in a single TIR channel and LST and utilizes simple linear regression. The model consists of a linearization of the radiative

transfer equation that maintains an explicit dependence on surface emissivity:

$$LST = A_i \frac{T_b}{\varepsilon} + B_i \frac{1}{\varepsilon} + C_i \quad (2.6)$$

where T_b is the TOA brightness temperature in the TIR channel, and ε is the surface emissivity for the same channel. The algorithm coefficients A_i, B_i and C_i are determined from linear regressions of radiative transfer simulations performed for 10 classes of TCWV (I = 1, …,10), ranging from 0 to 6 cm in steps of 0.6 cm, with values of TCWV above 6 cm being assigned to the last class.

The calibration database used to obtain the coefficients of Equation (2.6) has been derived using a dataset of air temperature, water vapor, and ozone profiles compiled.

2.4.2 Modified Workflow in GEE

Basically, the workflow that describes the processing chain of retrieved SST distribution at each observation time can be completed based on SMW algorithm and datasets provided by GEE.

Compared with the approach process proposed by Sofia L. Ermida et al [16], the workflow described in this study is dedicated to SST retrieval, complete image display and batch export which were not considered in previous studies. Rather than selecting the first feature from the image dataset in a specific date range to be the result image in the previous code, mosaicking is utilized in this workflow which refers to the process of spatially assembling image datasets to produce a spatially continuous image.

In the processing chain, first, the data range, the Landsat satellite number and the region of interest should be provided. Based on this information, the next step is to load

collections of TOA brightness temperatures (BT) and Surface Reflectance (SR) respectively which is the beginning of the main module in the processing chain. Cloud masking is performed for both using the quality information bands. Regarding each TOA BT image based on each observation time, the two closest NCEP datasets are interpolated. FVC value can be calculated by NDVI values which are computed by band parameters as described in 2.3.3. These FVC values are then used together with previously computed ASTER emissivity values for the bare ground to obtain the corresponding Landsat emissivity. Then, the SMW algorithm is applied to the TOA TB of the Landsat TIR band, the algorithm coefficients are mapped onto the Landsat image based on TWVC from NCEP and taking 10 classes. Finally, after combining spatially overlapping images into a single image based through mosaicking and applying the land mask 'JRC Monthly Water Recurrence' to the retrieved result, complete SST distribution can be displayed and exported in batches. The workflow of the processing chain in GEE is shown in Fig. 2.7. The blue text indicates coded functions in modules. The gray text indicates GEE datasets used in the production.

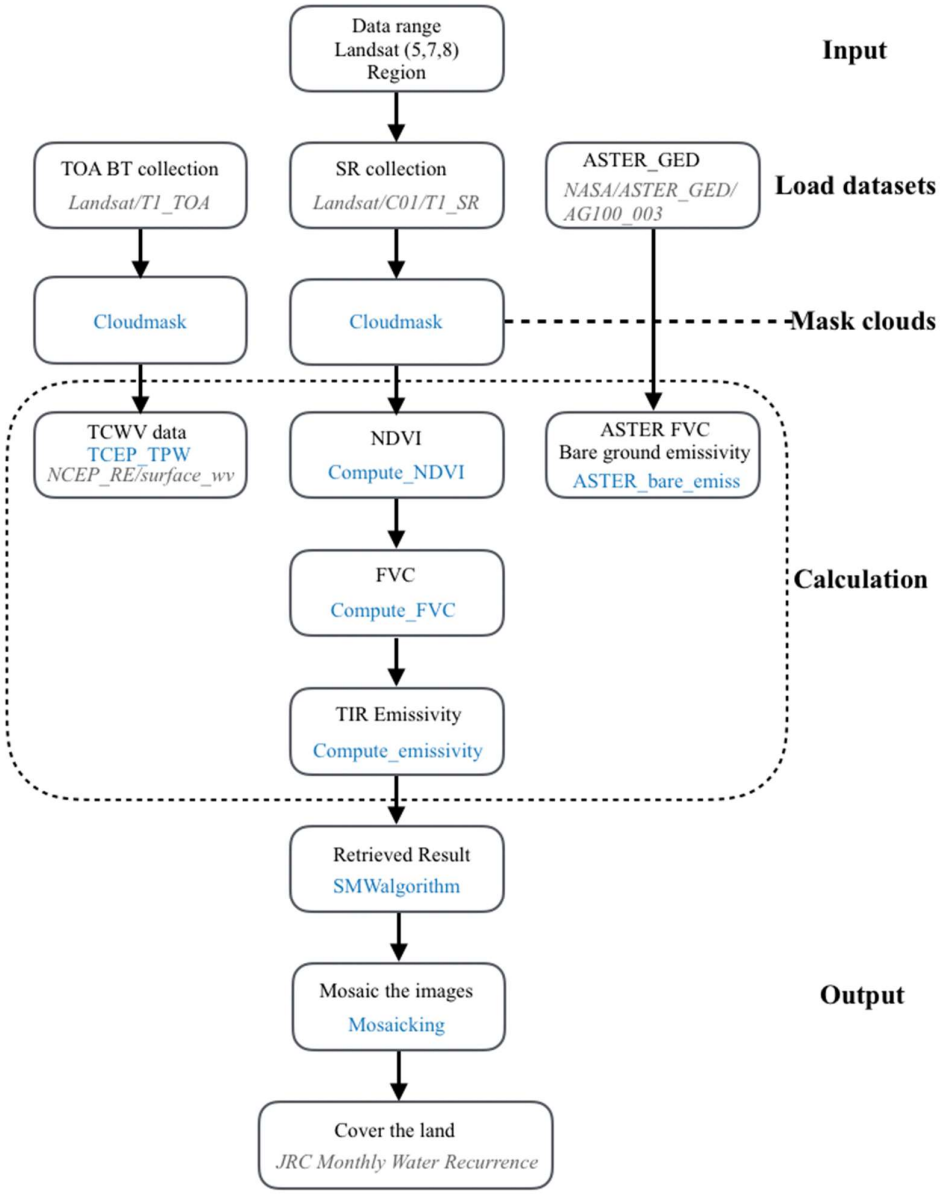

Fig. 2.7 Improved workflow in GEE [28]

2.4.3 Temporal and Spatial Analysis

Generally, each pixel of the image collection contains a time series, and it would be

possible to obtain a time series of each pixel with monotonic trends.

However, the date when Landsat 8 can take pictures with better cloud conditions varies every year, the annual average sea surface temperature calculated with satellite data can have a large error with the real value in this case. In terms of sea surface temperature trends, the results of using distribution images to show the spatio-temporal variation of annual mean sea surface temperature over 8 years will become quite unreliable.

In this study, the distribution of the average SST in each of the four seasons over the eight years will be calculated,

2.4.4 Spatial Gradient Calculation

The investigation of the spatio-temporal properties of SST gradients has become an important field of study in physical oceanography, due to the influence of ocean fronts on weather and climate patterns as well as on ocean primary production [28]. Based on the SST values retrieved through GEE, the magnitude of the SST gradient at location (i, j) in the lat / lon grid is calculated using a finite central difference scheme in the zonal and meridional directions as follows:

$$|SST(i,j)| = \left(\left[\frac{SST(i+1,j) - SST(i-1,j)}{d_{i+1,j}^{i-1,j}} \right]^2 + \left[\frac{SST(i,j+1) - SST(i,j-1)}{d_{i,j+1}^{i,j-1}} \right]^2 \right)^{1/2} \quad (2.7)$$

where $d_{i-1,j}^{i+1,j}$ represents the distance in kilometres between grid points (i+1, j) and (i-1, j).

2.4.5 Seagrass Meadows Management

Rising water temperatures tend to increase rates of seagrass respiration (using up oxygen) faster than rates of photosynthesis (producing oxygen), which makes them more susceptible to grazing by herbivores. Increased temperature also increases seagrass light requirements, influences how quickly seagrasses can take up nutrients in their environment and can make seagrasses more susceptible to disease. As seagrasses fulfill an important role in the quality of the coastal waters, it is necessary to predict the condition of seagrass meadows based on seawater temperature data.

The applicability of Landsat imagery based efficient temperature monitoring to seaweed and seagrass habitats will be considered and validated using Tokyo Bay and Hakata Bay as examples through SST mapping.

3 Results and Discussion

3.1 SST Retrieval Results Displayed on GEE

Eight years (2013-2020) original Landsat 8 data has been obtained and calculated for SST retrieval based on the GEE platform, automatically in this study. Since Landsat satellites image the entire Earth every 16 days, as well as the relatively bad cloud cover condition above Tokyo Bay, images that can be utilized for further discussion are almost less than 8 each year, as shown in Table. 3.1

Table. 3.1 Date acquisition and cloud cover (%) of Landsat 8 images obtained

No.	Cloud Coverage(%)	Date Acquisition
1	36.75	2013/4/26
2	16.07	2013/5/12
3	12.94	2013/8/16
4	16.95	2013/9/1
5	1.02	2013/9/17
6	29.98	2013/10/3
7	3.33	2013/11/20
8	6.42	2014/1/7
9	6.46	2014/1/23
10	11.27	2014/3/12
11	4.21	2014/3/28
12	1.83	2014/5/31
13	16.48	2014/6/16
14	17.5	2014/7/2
15	14.83	2014/8/3
16	17.58	2014/8/19
17	17.58	2014/11/23
18	5.52	2014/12/9
19	16.28	2015/1/10
20	3.76	2015/3/31
21	9.17	2015/4/16
22	1.93	2015/5/2
23	10.43	2015/7/21
24	3.54	2015/8/6
25	0.91	2015/10/9
26	2.27	2015/10/25
27	3.58	2016/3/17
28	31.86	2016/4/18
29	30.17	2016/5/4
30	30.37	2016/7/7

No.	Cloud Coverage(%)	Date Acquisition
31	50.09	2016/9/9
32	5.2	2016/10/27
33	19.55	2017/1/15
34	4.54	2017/2/16
35	5.2	2017/3/20
36	4.5	2017/4/5
37	2.28	2017/5/23
38	3.63	2017/7/10
39	20.46	2017/12/17
40	27.38	2018/4/8
41	28.41	2018/8/30
42	2.18	2018/10/1
43	6.45	2018/11/2
44	37.64	2018/12/4
45	6.58	2019/1/5
46	8.59	2019/1/21
47	16.27	2019/4/11
48	14.2	2019/8/1
49	15.94	2019/8/17
50	44.13	2019/9/2
51	62.52	2019/10/4
52	0.64	2019/11/5
53	3.91	2019/11/21
54	8.59	2020/2/9
55	3.66	2020/4/29
56	3.66	2020/5/15
57	32.52	2020/8/3
58	9.69	2020/8/19
59	25.61	2020/9/4
60	4.29	2020/11/23
61	10.23	2020/12/25

All the retrieved results can be directly shown on the GEE map with a mask covering the non-study area. In addition, it is likely to continue to process the results in ArcGIS as the results can be output as Geotiff files. Here are the retrieved results shown on the GEE map after running the codes only in 2019 and 2020 (Fig. 3.1).

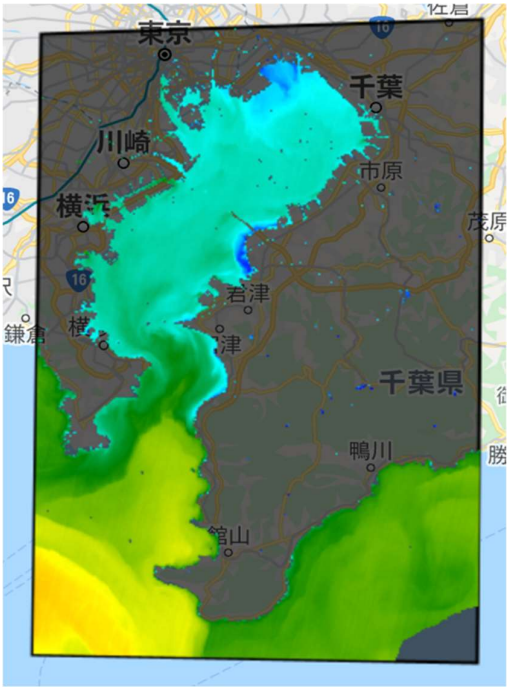

(a)2019.1.5

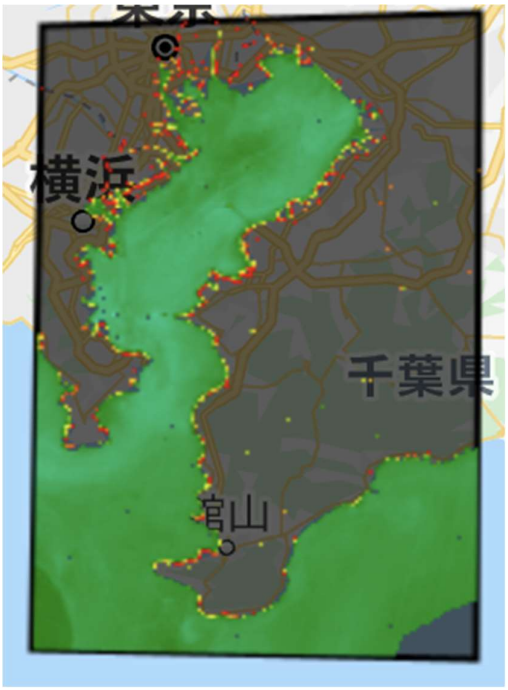

(b)2019.1.21

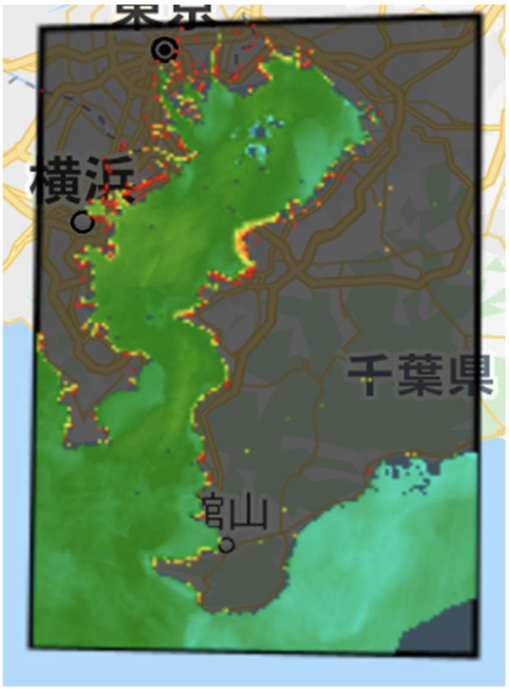

(c)2019.4.11

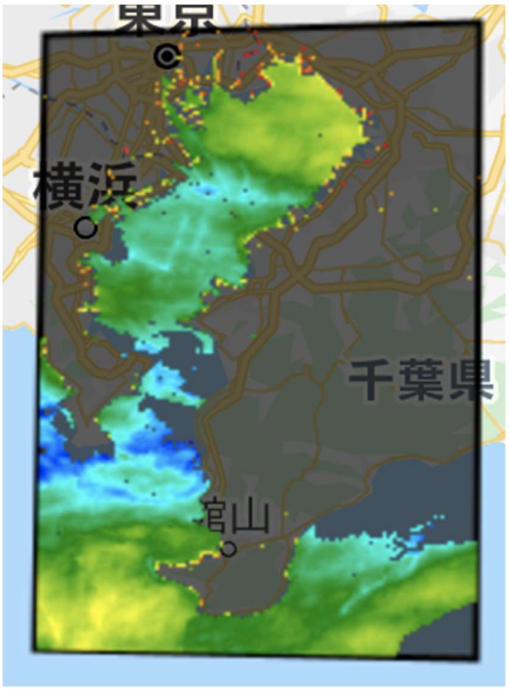

(d)2019.8.1

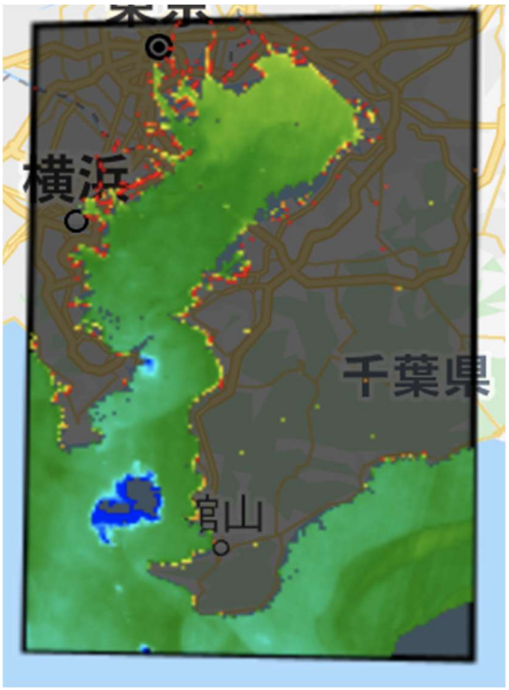

(e)2019.8.17

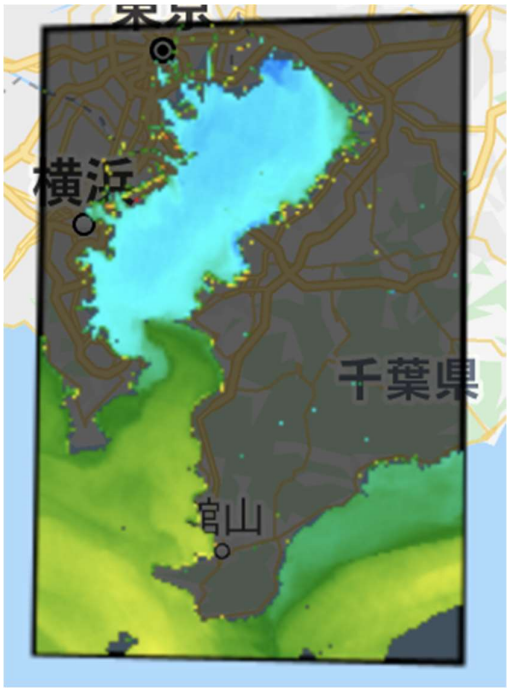

(f)2019.9.2

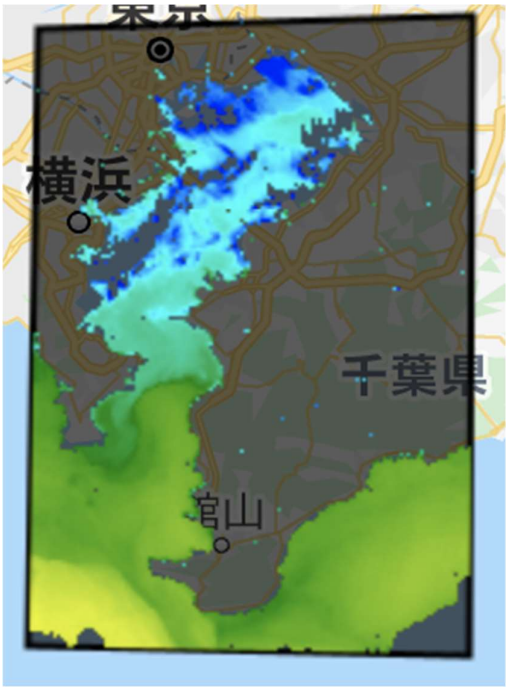

(g)2019.10.4

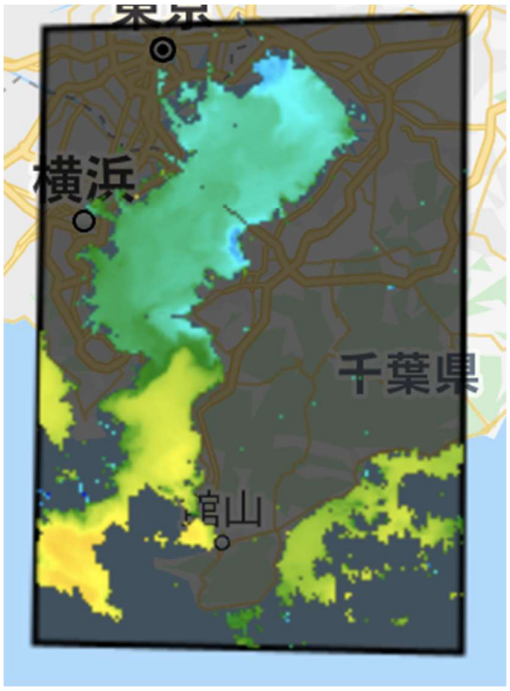

(h)2019.11.5

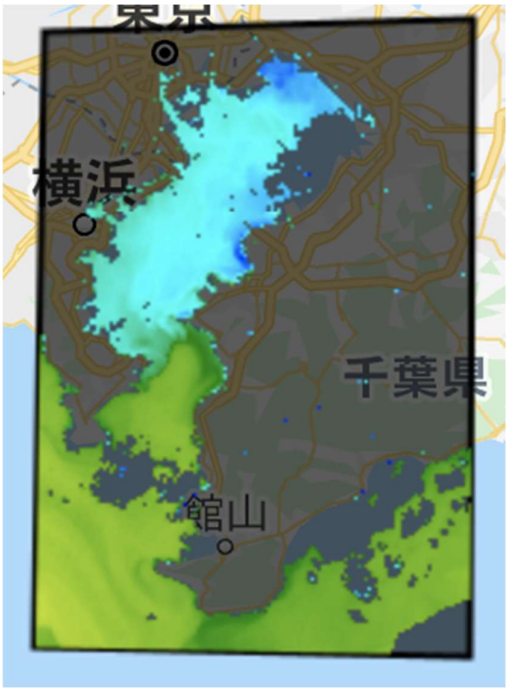

(i)2019.11.21.

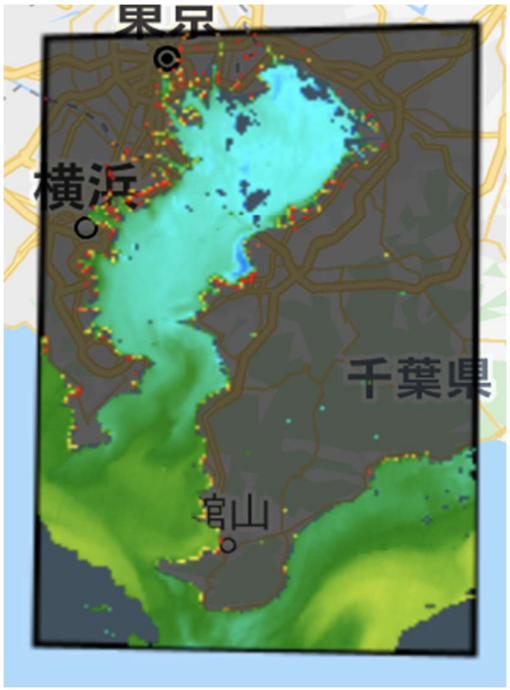

(j)2020.2.9

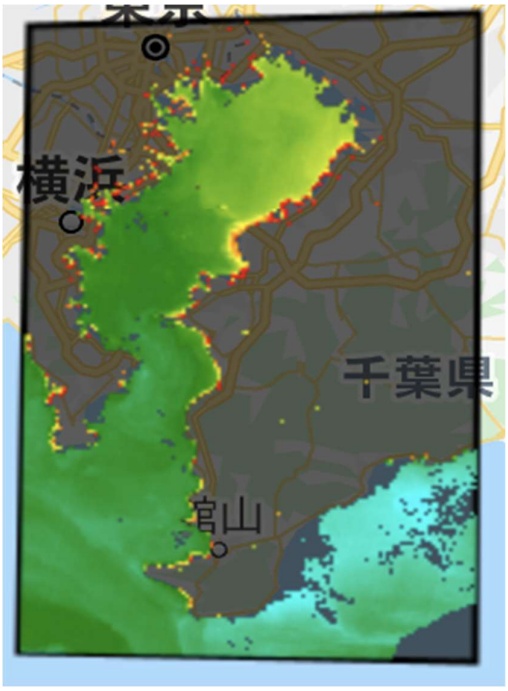

(k)2020.4.29

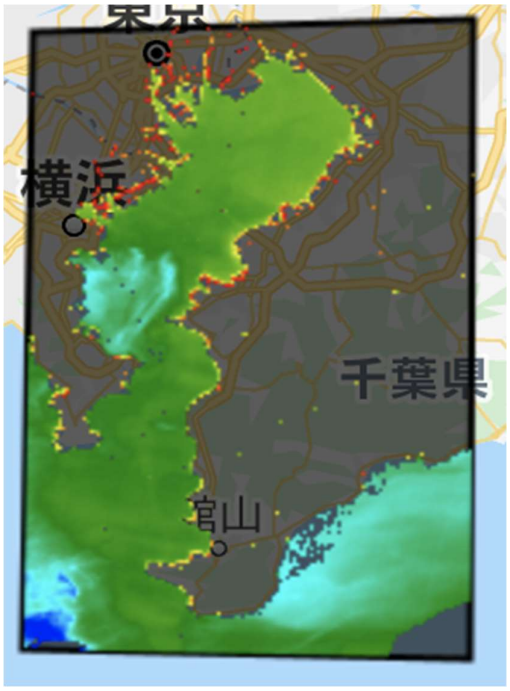

(l)2020.8.3

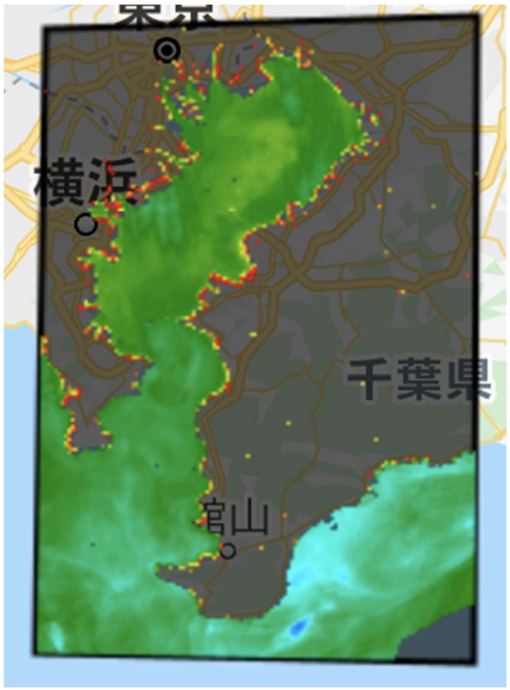

(m)2020.8.19

(n)2020.9.4

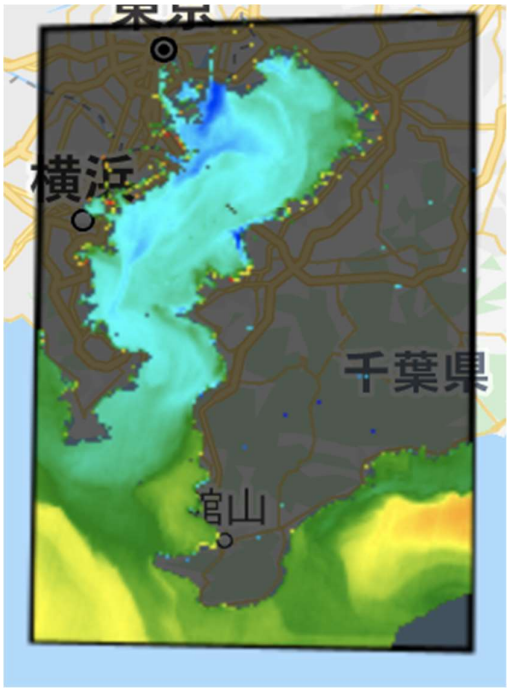

(o)2020.11.23

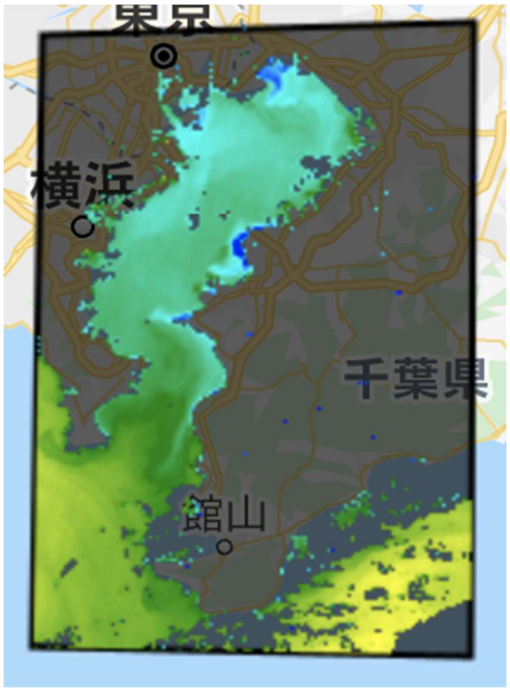

(p)2020.12.25

Fig. 3.1 Retrieved SST results on GEE map in 2019 and 2020

The color bar of the display of the maps is the same that the color from blue to red represents the temperature from low to high.

From the maps in 2019 and 2020, we can come to three conclusions qualitatively.

It would be possible to utilize Landsat 8 TIR sensor to discuss sea surface temperature changes since the SST distribution pattern can be clearly shown on the maps.

The distribution of sea surface temperature in Tokyo Bay varies with seasons. Especially in winter, SST in the bayhead is relatively lower than that in the bay mouth, which is likely to be affected by higher open ocean water.

Overall, sea surface temperature nearshore is higher than that in the center of the bay. However, it is not so convenient to change the color bar, show the specific color range and value using GEE. As a result, such work will be completed through ArcGIS.

3.2 Improvement with Modified Code

In the method provided by Sofia L. Ermida et al [16], they select the first feature from the image dataset as the result of the display, however, the result cannot show properly and completely especially when the defined date range is short. With the mortification and improvement of the code, there is no missing result regardless of the length of the input date interval. Images in Fig. 3.2 show the obvious difference between results processed by Sofia L. Ermida code (left) and modified code (right) on 2018.8.14 as an example. The modified code can greatly improve the problem that the results are not displayed correctly.

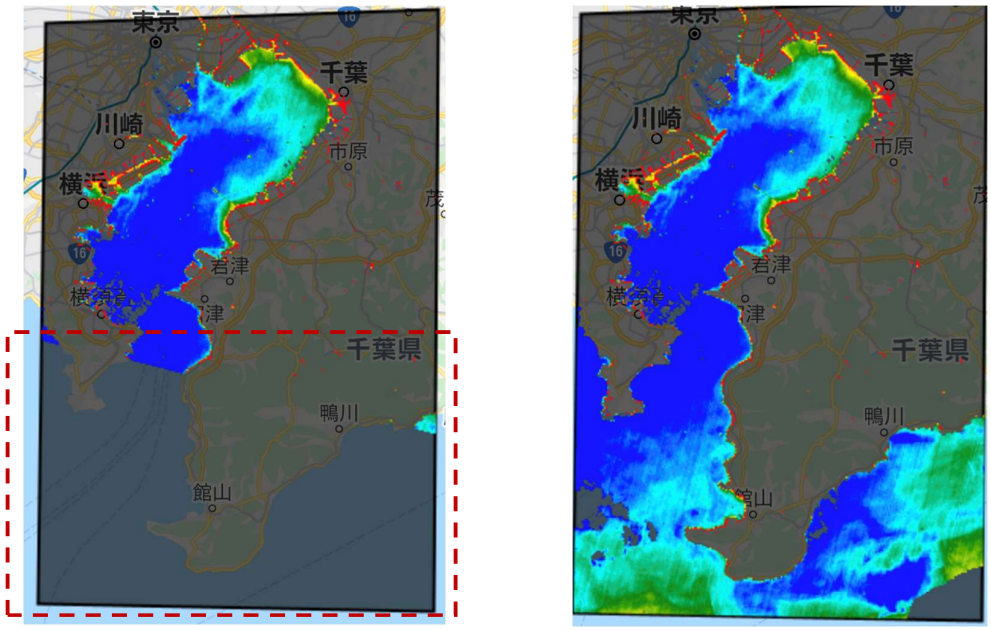

(a) (b)

Fig. 3.2 Result processed by Sofia L. Ermida code (a)
Result processed by modified code (b)

3.3 Validation with Monitoring Data

Validation work was carried out for SST, using data from satellite retrieval results and monitoring station systems of the corresponding Tokyo Bay. The observation sites are Urayasu, Kemigawa, Kawasakijinnkoutou, Chiba port No.1 light gauge, Chiba gauge, Nakanose, Kaneda Bay and Tomiura Bay. All the observation sites are equipped with sensors that can collect the seawater temperature data at the surface, middle and bottom simultaneously. Since the study is focusing on the coastal area, it is necessary to assess the accuracy of retrieved SST along coastlines.

Urayasu Monitoring Site is located at 35°38’24” N, 139°56’30” E, which is quite close

to the coastline near Urayasu City in the bayhead. The site provides hourly data from 2010.4.1 to the present.

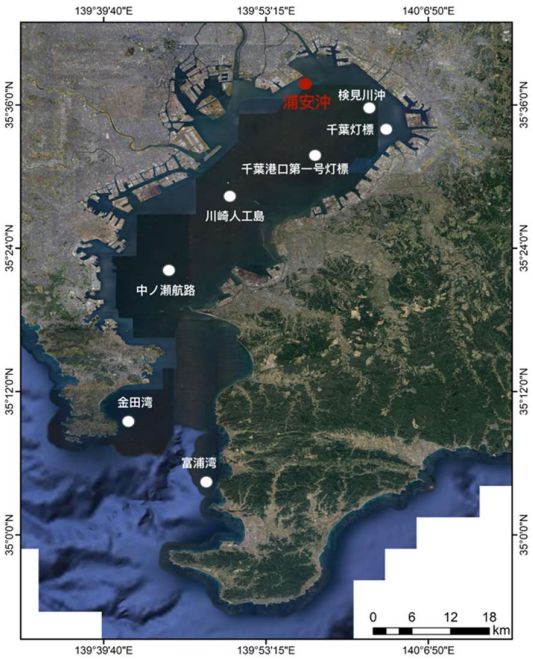

Fig. 3.3 Location of observation sites (source: google map)

A total of 61 images were identified from 2013 to 2020. Fig. 3.4 shows the number of images in each year.

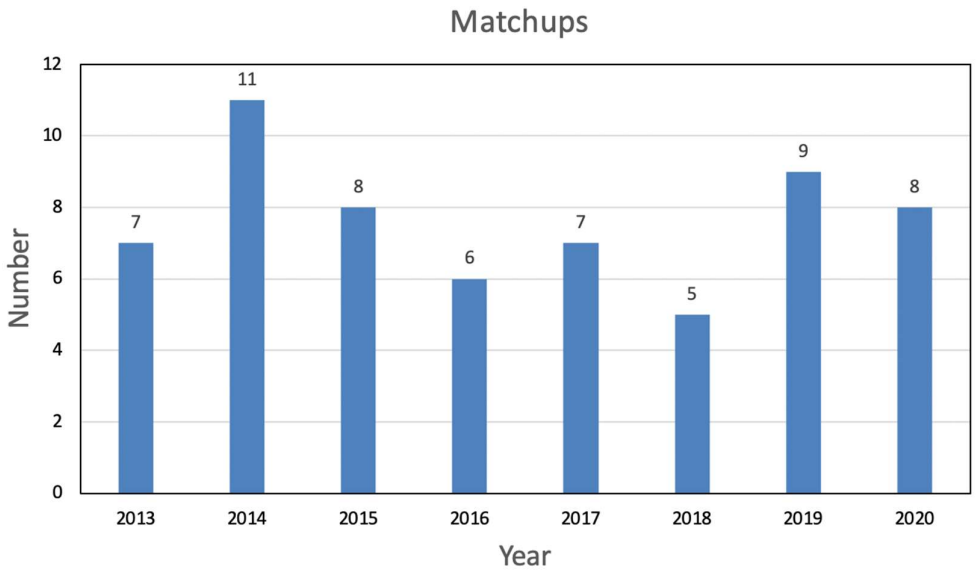

Fig. 3.4 The number of matchups each year

In this analysis, the linear regression analysis is applied to evaluate the linear relationships between retrieved SST and SST observed, and the results show the R^2 value in the range of 0.9637-0.9866, which indicates a higher relationship of retrieved SST for all monitoring stations.

Table. 3.2 R^2corresponding to different sites

Monitoring Station	R^2
浦安沖(near the coast)	0.9866
検見川沖	0.9788
川崎人工島	0.9704
千葉灯標	0.9691
千葉港口第一号灯標	0.9858
中ノ瀬航路	0.9637
金田湾	0.9782
富浦湾	0.9771

Fig. 3.5 shows SST cross-validation using linear regression relationship using SST

derived (Landsat 8 TIRS) and SST observation data during 2013–2020. Each monitoring data was matched with the nearest Landsat SST within a temporal and spatial window of 1 hour and 1 km centered at the monitoring location.

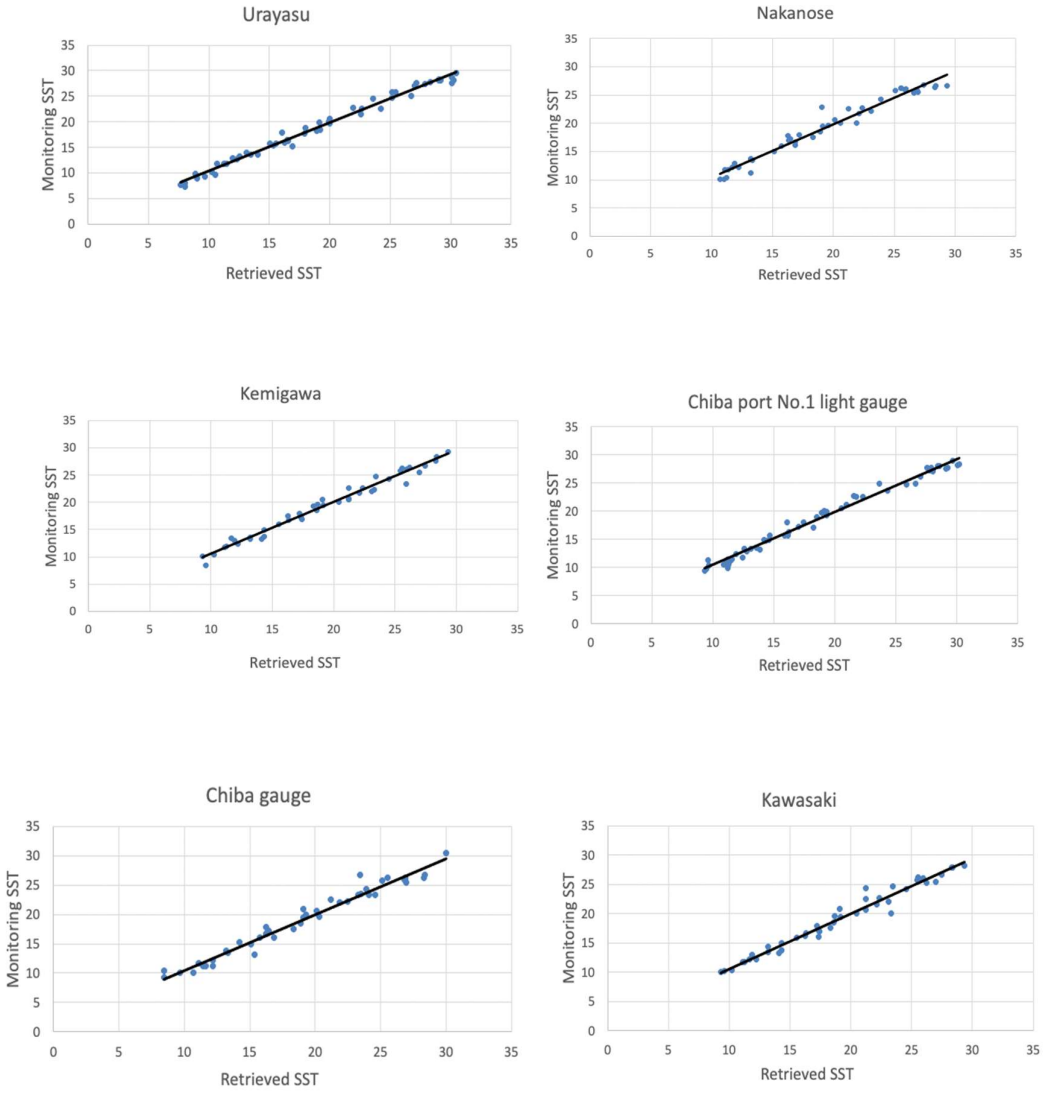

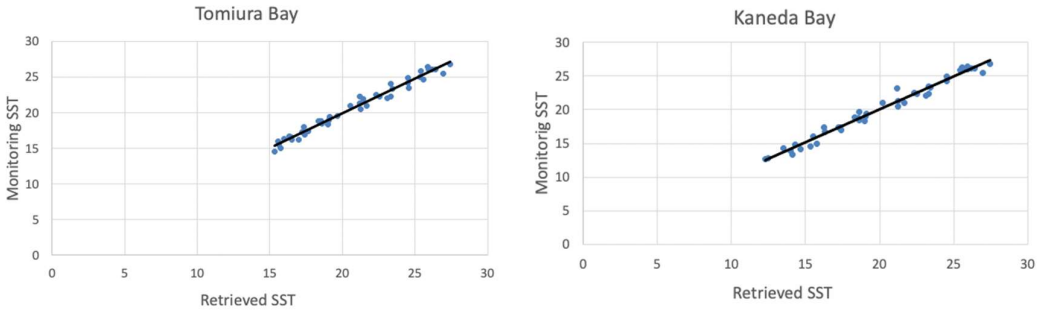

Fig. 3.5 SST cross-validation

Obviously, relatively large difference exists in SST cross-validation, which can be explained by the cloud condition on specific dates. As has been shown in Table 3.1 in Section 3.1, due to the data limitation, not all data with bad cloud conditions were screened out, and parts of Tokyo Bay were obscured by cloud cover on some days. As a result, cloud coverage affected the calculation results and their accuracy to some extent.

3.4 SST Temporal and Spatial Variation

In this part, a detailed discussion is made to explore the characteristics of sea surface temperature changes depending on four seasons and focus on the spatial distribution.

3.4.1 Spatio-Temporal Variation

Fig. 3.6 below shows the distribution of the average SST in each of the four seasons over the eight years, which has been directly calculated, and output based on GEE. The average SST images of December, January and February stand for winter, while the average SST images of March, April and May represent spring. Sequentially, average results of June, July and August, which of September, October and November stand for autumn.

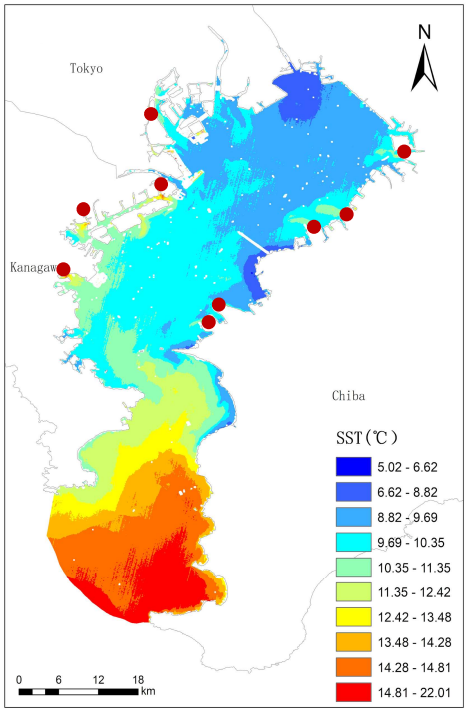

(a)winter

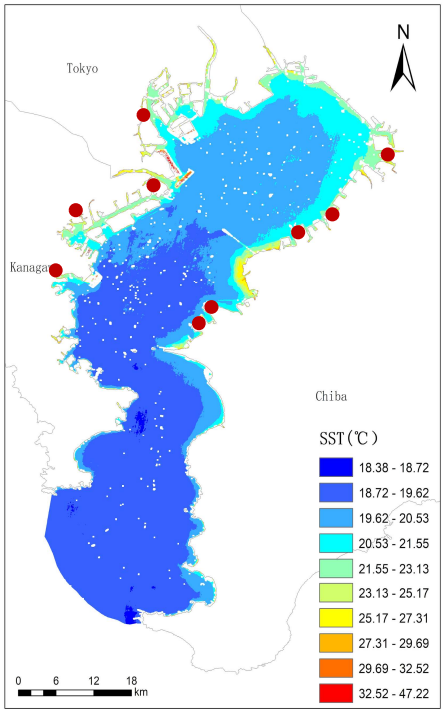

(b)spring

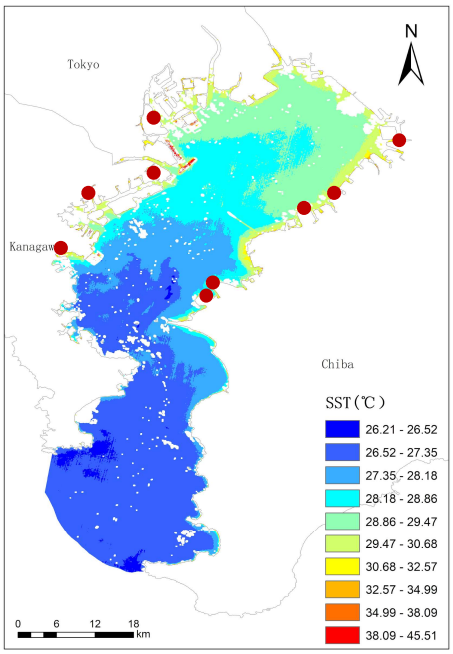

(c)august

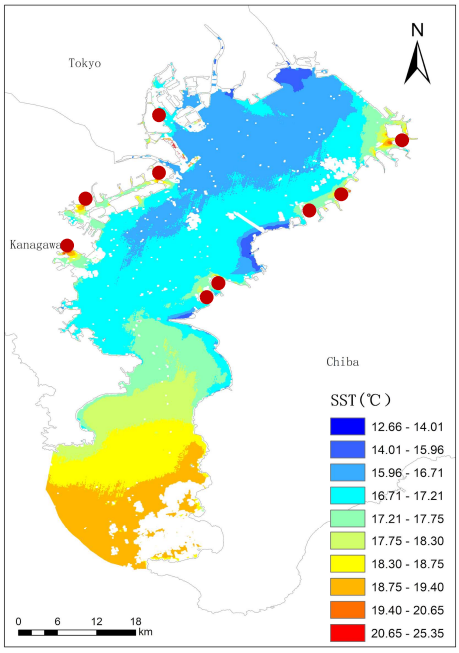

(d)autumn

Fig. 3.6 SST distribution in four seasons

(Red circles represent thermal power plants)

As observed from four images of average SST distribution in four seasons, they clearly display the seasonal variability of the spatial patterns of SST in Tokyo Bay. We can come to several conclusions qualitatively and quantitatively.

First, SST at the head of the bay (north) is lower than that at the mouth of the bay (south) in winter, and vice versa in summer. From the seafloor topography data obtained from the archives of the Japan Oceanographic Data Center, it can be found that the bay deepens gradually from the head to the mouth, which results in a total heat capacity of the water column. As a result, SST at the head becomes lower in winter and higher in summer than that at the mouth. In addition, SST is greatly influenced by water exchange between the bay and the Pacific Ocean. In winter, SST in the northwestern portion of the bay tends to be low because of the cool river flowing into the bay.

Contrary to winter and summer, spring and autumn are the transitional seasons. The SST spatial distribution pattern in spring and autumn is very different from that of winter and summer. As seen from Fig. 3.6, the temperature is higher in the coastal shallows and lower in the profundal zone in spring. In autumn, the SST is much lower in the northwest of the bay head, while in winter the SST is lower in the northeast of the bay.

Second, the SST in Sanbanze tidal flat which is located near the estuary of Edo River and Banzu tidal flat near Kimitsu city is lower than surrounding water areas in winter, while the SST in the same area is higher than other adjacent areas in summer. We can see that the temperature difference between the tidal flat and the surrounding area can reach up to 3 degrees from the color ramp in four images. The main reason for these

interesting patterns is that the waters of the Sanbanze tidal flat and Banzu tidal flat are relatively shallow, mainly from 0m depth to -5m [29] which indicates that the temperature of shallow water is easily affected by the air temperature.

The third, but key point in this study is that the effect of thermal power plant drainage on the SST around the coast keeps greatly visible in autumn and winter. The SST distribution patterns reveal that SST of the areas that are adjacent to Isogo Thermal Power Plant, Yokohama Power Plant, Kawasaki Power Plant, Shinagawa Power Plant, Chiba Thermal Power Plant, Anegasaki Power Plant, Sodegaura Power Plant, Kimitsu Kyodo Power Plant and Futtsu Power Plant shows a significant rise. The thermal plume expands outward and decreases from the discharge outlet of each thermal power plant. The farthest distances of thermal plumes (>2 degrees than offshore SST) are about 500m-2km. The temperature difference between the drain outlet and the offshore water can be up to 7 degrees in winter and 5 degrees in autumn. Although nearshore SST is generally higher than offshore SST in spring and summer, the effect of thermal power plant discharge on surrounding SST does not appear to be significant. Accordingly, areas around Kawasaki will be enlarged to make further discussed.

(a)

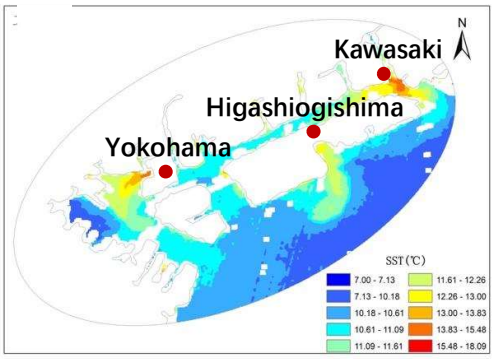

(b)winter

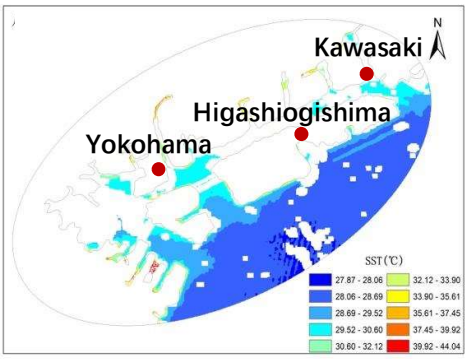

(c)summer

Fig. 3.7 Water areas around Kawasaki(a) (source: google map)
SST distribution around Kawasaki in winter (b) and summer (c)

As stated above, the thermal plumes discharged from Yokohama Power, Higashiogishima Power Plant and Kawasaki Power Plant are extremely visible in winter, whereas thermal discharge does not cause any significant increase in SST around power stations in summer (Fig. 3.7).

3.4.2 Spatial Gradient Variation

The characteristics of the SST spatial gradient in these four images are consistent with the results shown in the previous section 3.3.2.

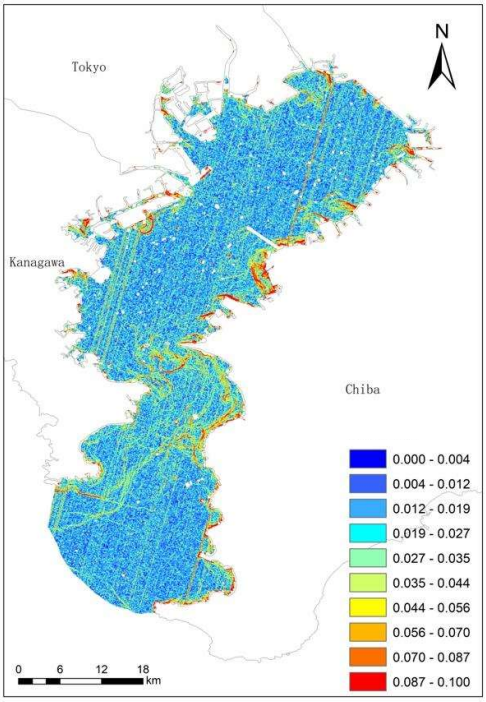

(a)winter

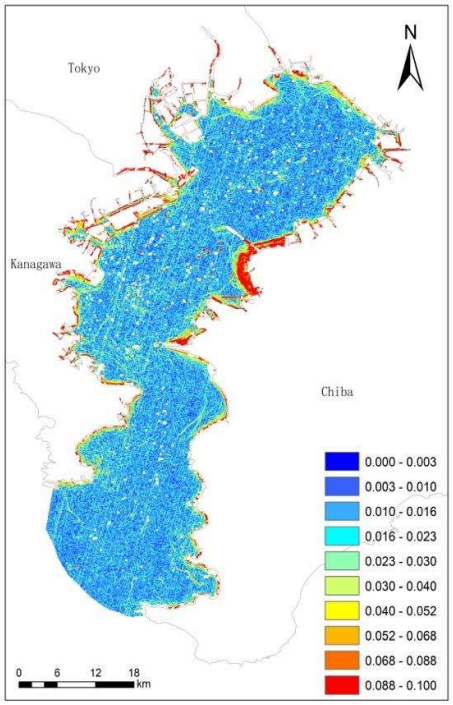

(b)spring

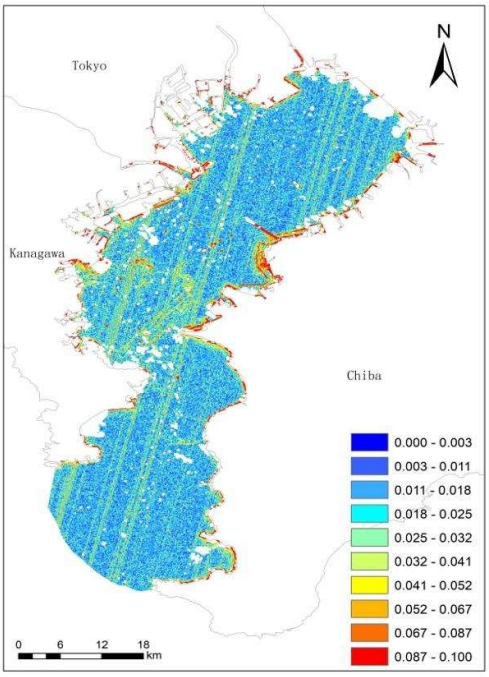

(c)august

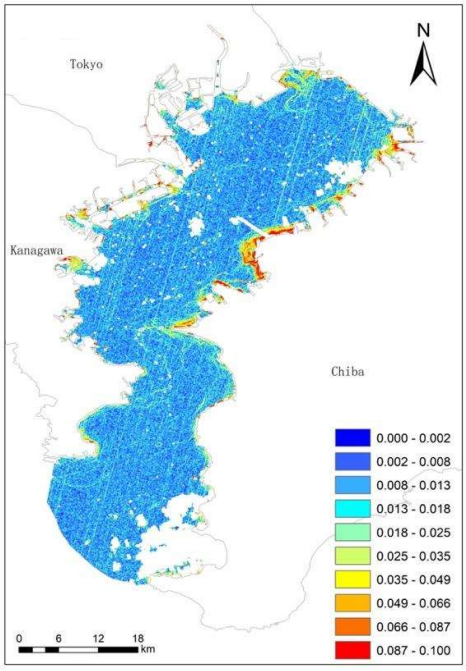

(d)autumn

Fig. 3.8 SST gradients in four seasons

The gradients along coastal areas, especially near the thermal power plants mentioned above and shallow water areas like Sanbanze tidal flat, Banzu tidal flat and Futtsu tidal flat are greater than those in other areas which means greater temperature change at the same distance. The SST spatial gradients are the greatest, ranging from 0.087-0.1 in Banzu tidal flat as well as Futtsu tidal flat.

Nevertheless, abnormal striping exhibits in the above four images. The USGS pointed out that due to sensor calibration problems, some of Landsat 8's bands have annoying stripe patterns, among which the stripes in the thermal bands are the most problematic. How to solve the stripe problem in the program or GEE should also be considered as one of the future works.

To be concluded in this part, although temporal data of Landsat 8 is limited, we can still analyze the temporal-spatial variation of SST via different seasons. The spatial pattern of SST varies in four seasons, which was probably affected by air temperature, precipitation, wind speed, and water depth. The usefulness of Landsat 8 for the analysis of SST changes over small-scale areas has been demonstrated in this study since the thermal plume discharged by thermal power plants can be clearly shown on the SST spatial distribution images and spatial gradient images which has a non-negligible impact on the water environment around the power plants especially in autumn and winter. The SST near the coast is higher totally compared with offshore SST. The SST values on SST distribution images are consistent with validation results as well. Along with such prerequisites that seaweed and seagrass meadows can be damaged by warm seawater temperature, Landsat 8 can be utilized for alerting seagrass and seaweed management along the coast without in-situ temperature monitoring buoys.

3.5 Discussion on seagrass meadows

In the previous section of this study, it has been demonstrated that Landsat 8 data can be processed efficiently by GEE, and the high resolution of the obtained SST profiles is sufficient to determine the influence of thermal discharge around the drainage of thermal power stations, so similarly Landsat 8 can be utilized to analyze seagrass conditions that also require high resolution and refer to coastal areas.

3.5.1 Futtsu Tidal Flat

Monitoring work of eelgrass beds in Futtsu site has been conducted each year by the Natural Environment Bureau of the Ministry of Environment. The accessible official investigation report in 2020 mentioned that eelgrass near the coastline has been on a markable downward trend since 2016, no eelgrass could be found in 2019. At the survey site about 800m offshore, where the water depth is deeper than -1m, eelgrass coverage recovered slightly in 2019. In addition, at the site about 1.1km offshore, where the water depth is deeper than -2 m, the distribution and cover of eelgrass increased significantly [30].

Fig. 3.9 shows the SST distribution around Cape Futtsu in the summer of 2019. It is worth noting that the SST near the shore is more than 30 degrees, which is not suitable for seagrass growth. One important reason for such high SST is the trend towards shallower water depth in nearshore areas in recent areas, in which case, SST is easily affected by air temperature. In terms of Futtsu tidal flat, in the intertidal zone, the water depth changes in a complex manner due to the presence of multiple sand bars, leading to irregular SST distribution patterns in the same month.

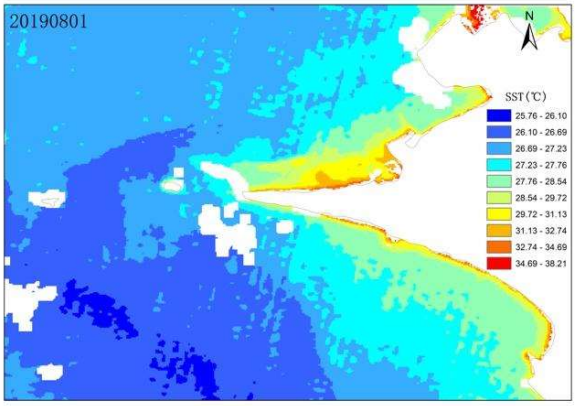

(a) 20190801

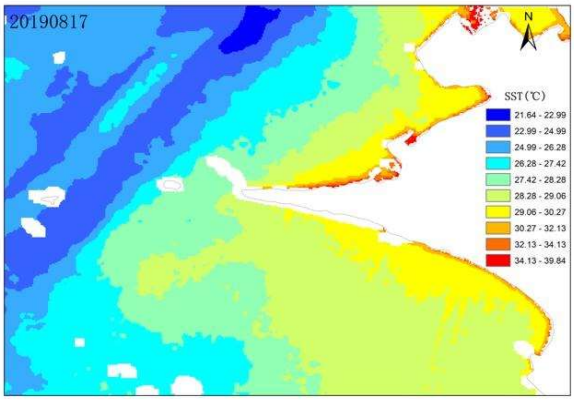

(b) 20190817

Fig. 3.9 SST distribution in Futtsu tidal flat

Table. 3.3 Tide level on 2019.8.1 and 2019.8.17

Spring Tide(20190801)		
Time	4:16	11:10
Tide Level	174cm	3cm

Spring Tide(20190817)		
Time	5:17	11:54
Tide Level	179cm	11cm

Table 3.3 shows tide level on each date, respectively. Tide level is the height of the sea surface measured from a fixed reference plane. The data was measured by Fort No.1 monitoring station near Futtsu. The images were taken at 10:00 a.m. +/- 15 minutes. Obviously, variations of SST in Futtsu tidal flat are associated with the tide. Moreover, the results of SST are consistent with what has been described through the survey results from official reports, especially the area extremely close to the shore.

3.5.2 Wajiro Tidal Flat

Wajiro tidal flat is considered important for its seagrass meadows management in marine environment preservation. A public report about a case study in Hakata Bay conducted by the Ministry of Environment mentions that the sudden disappearance of seagrass meadow was observed in 2014 and high seawater temperature in 2013 has been considered as the most important factor that results in such phenomenon [31]. It could be quite easy to acquire air temperature data from Japan Meteorological Agency that average air temperature in August in 2013 reached up to 30 degrees, while in 2012, the average value was only 26 degrees. However, unlike Tokyo Bay, few public monitoring stations in Hakata Bay can provide hourly or monthly SST data in specific locations to discuss the causes of the disappearance of seagrass meadows. Under such circumstances, high-resolution satellite imagery could be greatly useful and efficient.

Fig. 3.10 shows the SST distribution in Wajiro Tidal Flat in August 2013 and 2012, respectively.

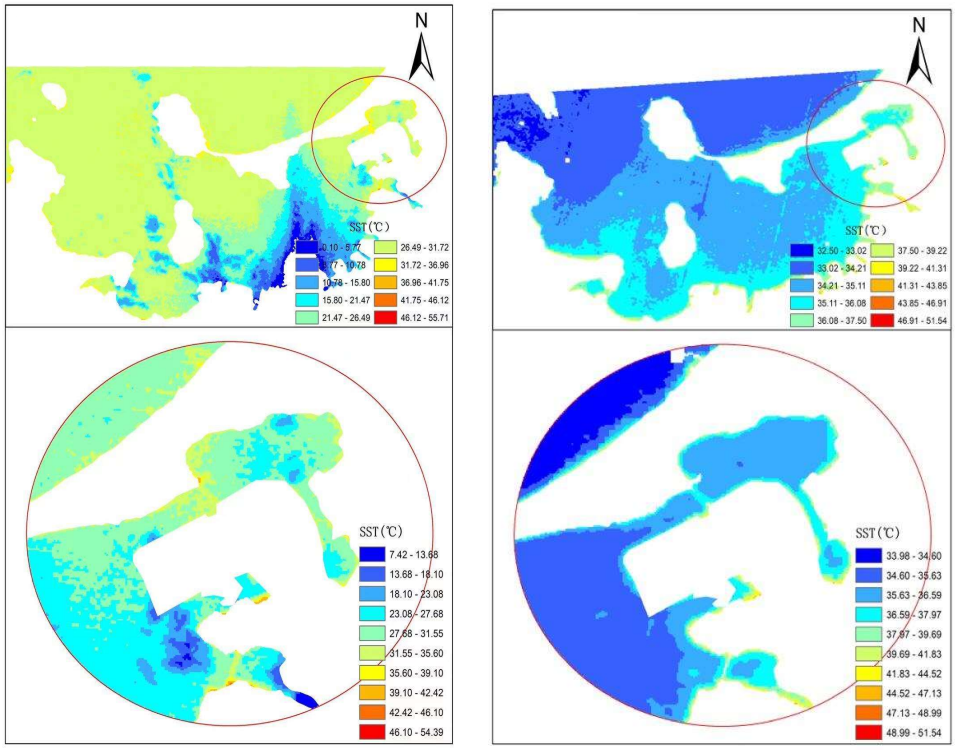

Fig. 3.10 SST distribution in Wajiro Tidal Flat in August 2013 (right) and 2012 (left)

By comparing the two images, we can clearly find the difference in SST value. The average SST in Wajiro tidal flat in 2013 was more than 35 degrees, however, the average value in 2012 was about 28 degrees. Since the data of Landsat is limited, there is no other data available except for the data with some areas of the images covered by clouds in August 2012. The accuracy of the dark blue area shown in Fig. 3.10 (left) is affected by the clouds, but SST in other areas and SST distribution tendency are still very reliable.

However, there is only one data in August 2012 and 2013 that can be utilized for discussion respectively due to the limitation of Landsat data, both of which were taken in the middle of August. Although these two results illustrate the difference between the SST in August 2012 and August 2013 to some extent, we still can't tell from one day's data that the average SST in August 2013 reached 30 degrees. Some other methods should

be developed to obtain more satellite data that also has high resolution to discuss such situations and possible factors.

To summarize, we must admit the applicability of Landsat 8 based on efficient temperature monitoring to seaweed and seagrass habitats along coastal areas since high-resolution imagery is most in need. However, its low frequency still imposes some limitations on analysis.

4 Conclusions

4.1 Conclusions

This study analyses the spatial-temporal variation in sea surface temperature from Landsat 8 TIR which has a higher resolution compared with other commonly used satellites. The main tool for processing satellite data and completing statistical calculation is Google Earth Engine which is an efficient online platform especially when it comes to processing several years of data.

The results and discussion sections can be concluded into several points.

The method that using GEE to process Landsat 8 has proved to be quick and automatic. Although Landsat 8 temporal data is limited, the temporal analysis still can be analyzed through seasonal analysis. Totally, the spatial pattern of SST varies in four seasons, which is mainly affected by topography and water exchange. In the coastal areas, the spatial pattern of SST in different seasons also indicates the influence of thermal power plants and water depth on SST. In this study, SST spatial gradients are also calculated through GEE automatically. The characteristics of SST spatial gradients are consistent with the above conclusions.

With two examples of Tokyo Bay and Hakata Bay, the SST distribution corresponds to seagrass beds' growth or disappearance condition. It has been proved that Landsat 8 using on GEE platform is applicable based efficient temperature monitoring and processing to seaweed and seagrass habitats management.

4.2 Prospect

As has been mentioned in this study, the biggest disadvantage of Landsat 8 is the relatively long revisiting period which limits the number of temporal data. Because of the obstacles that the absence of a single sensor that provides images free of charge contemplating both characteristics (high frequency and detailed monitoring), it is necessary to apply different satellites to different targets flexibly and generate hybrid products at a high/medium spatial resolution and high temporal resolution.

Some studies have introduced how to combine Landsat data and MODIS data, in order to create fusion images which both have high resolution and frequency. However, in terms of SST, the results of such work in previous studies are not so realistic.

In my consideration, the future research topic could focus on how to complete such fusion work based on GEE using Landsat 8 data and other satellite data such as MODIS and Sentinel-3 which have short revisiting days. The advantage of GEE that it can process large amounts of data and output automatically should be utilized for long-term trending analysis of SST, especially along coastlines. The topic of the applicability of such work to Tokyo Bay, where cloud conditions are not good could also be validated and discussed.

Reference

[1] O. Tracks, "Sea Surface Temperature." https://oceantracks.org/library/oceanographic-factors/sea-surface-temperature.

[2] Qiu, B. "Kuroshio And Oyashio Currents," *Encycl. Ocean Sci.*, pp. 1413–1425, 2001, doi: 10.1006/rwos.2001.0350.

[3] Okuda, K. "Coastal Environment and Seaweed-bed Ecology in Japan," *Kuroshio Sci.*, vol. 2, no. 1, p. 6, 2008.

[4] Federation of Electric Power Companies, "Mechanism of Nuclear Power Generation." https://www.fepc.or.jp/english/nuclear/power_generation/mechanism/index.html.

[5] Huang, F., Lin, J. and Zheng, B. "Effects of thermal discharge from coastal nuclear power plants and thermal power plants on the thermocline characteristics in sea areas with different tidal dynamics," *Water (Switzerland)*, vol. 11, no. 12, 2019, doi: 10.3390/w11122577.

[6] Sendai nuclear power station, "About thermal discharge from nuclear power plants." http://www.kyuden.co.jp/sendai_topix_onhaisui1.html.

[7] Chen, C., Shi, P. and Mao, Q. "Application of remote sensing techniques for monitoring the thermal pollution of cooling-water discharge from nuclear power plant," *J. Environ. Sci. Heal. - Part A Toxic/Hazardous Subst. Environ. Eng.*, vol. 38, no. 8, pp. 1659–1668, 2003, doi: 10.1081/ESE-120021487.

[8] World Meteorological Organization, "Essential Climate Variables." https://public.wmo.int/en/programmes/global-climate-observing-system/essential-climate-variables.

[9] García, M. J. L. "SST comparison of AVHRR and MODIS time series in the Western Mediterranean Sea," *Remote Sens.*, vol. 12, no. 14, pp. 1–12, 2020, doi: 10.3390/rs12142241.

[10] National Center for Atmospheric Research, “SST DATA SETS: OVERVIEW & COMPARISON TABLE.” https://climatedataguide.ucar.edu/climate-data/sst-data-sets-overview-comparison-table.

[11] Qin, Z., Karnieli, A. and Berliner, B. “A mono-window algorithm for retrieving land surface temperature from Landsat TM data and its application to the Israel-Egypt border region,” *Int. J. Remote Sens.*, vol. 22, no. 18, pp. 3719–3746, 2001, doi: 10.1080/01431160010006971.

[12] Jiménez-Munoz, J. C and Sobrino, J. A. “A generalized single-channel method for retrieving land surface temperature from remote sensing data,” *J. Geophys. Res. Atmos.*, vol. 108, no. 22, 2003, doi: 10.1029/2003jd003480.

[13] Sobrino, J. A., Sobrino, J. C., Jiménez-Muñoz and Paolini, L. “Land surface temperature retrieval from LANDSAT TM 5,” *Remote Sens. Environ.*, vol. 90, no. 4, pp. 434–440, 2004, doi: 10.1016/j.rse.2004.02.003.

[14] Dash, P., Göttsche, F. M., Olesen, F. S. and Fischer, H. “Land surface temperature and emissivity estimation from passive sensor data: Theory and practice-current trends,” *Int. J. Remote Sens.*, vol. 23, no. 13, pp. 2563–2594, 2002, doi: 10.1080/01431160110115041.

[15] Chen, X. L., Zhao, H. M., Li, P. X. and Yin, Z. Y. “Remote sensing image-based analysis of the relationship between urban heat island and land use/cover changes,” *Remote Sens. Environ.*, vol. 104, no. 2, pp. 133–146, 2006, doi: 10.1016/j.rse.2005.11.016.

[16] Ermida, S. L., Soares, P., Mantas, V., Göttsche, F. M. and Trigo, I. F. “Google earth engine open-source code for land surface temperature estimation from the landsat series,” *Remote Sens.*, vol. 12, no. 9, pp. 1–21, 2020, doi: 10.3390/RS12091471.

[17] Huang, S. J., Te Lin, J., Lo, Y. T., Kuo, N. J. and Ho, C. R. “The coastal sea surface temperature changes near the nuclear power plants of northern Taiwan observed from satellite images,” *Ocean. 2014 - Taipei*, pp. 2–6, 2014, doi:

10.1109/OCEANS-TAIPEI.2014.6964547.

[18] Lin, J., Zou, X., Huang, F. and Yao, Y. “Quantitative estimation of sea surface temperature increases resulting from the thermal discharge of coastal power plants in China,” *Mar. Pollut. Bull.*, vol. 164, no. January, 2021, doi: 10.1016/j.marpolbul.2021.112020.

[19] I. JERA Co., “Futtsu Thermal Power Station.” https://www.jera.co.jp/english/business/thermal-power/list/futtsu.

[20] Yamakita, T., Watanabe, K. and Nakaoka, M. “Asynchronous local dynamics contributes to stability of a seagrass bed in Tokyo Bay,” *Ecography (Cop.).*, vol. 34, no. 3, pp. 519–528, 2011, doi: 10.1111/j.1600-0587.2010.06490.x.

[21] U.S. Geological Survey, “Landsat Missions.” https://www.usgs.gov/core-science-systems/nli/landsat/landsat-8?qt-science_support_page_related_con=0#qt-science_support_page_related_con.

[22] U.S. Geological Survey, “Using the USGS Landsat Level-1 Data Product.” https://www.usgs.gov/core-science-systems/nli/landsat/using-usgs-landsat-level-1-data-product.

[23] Kalnay, E., Kanamitsu, M., Kistler, R., Collins, W., Deaven, D. and Gandin, L. “The NCEP / NCAR 40-Year Reanalysis Project,” 1996.

[24] Hulley, G. C., Hook, S. J., Abbott, E., Malakar, N., Islam, T. and Abrams, M. “The ASTER Global Emissivity Dataset (ASTER GED): Mapping Earth’s emissivity at 100 meter spatial scale,” *Geophys. Res. Lett.*, vol. 42, no. 19, pp. 7966–7976, 2015, doi: 10.1002/2015GL065564.

[25] Jiménez-Muñoz, J. C., Sobrino, J. A., Plaza, A., Guanter, L., Moreno, J. and Martínez, P. “Comparison between fractional vegetation cover retrievals from vegetation indices and spectral mixture analysis: Case study of PROBA/CHRIS data over an agricultural area,” *Sensors*, vol. 9, no. 2, pp. 768–793, 2009, doi: 10.3390/s90200768.

[26] ESRI Japan, “Data of Administrative District.”

https://www.esrij.com/products/japan-shp/.

[27] Tokyo Bay Environmental Information Center, “Continuous Monitoring of Water Quality in Tokyo Bay.” https://www.tbeic.go.jp/MonitoringPost/Top.

[28] Boualia, M., Polito a , P. S., Satoa , O. T., Bernardoa, P. S. and Vazquez-Cuervob, J. “The impact of cloud masking on the climatology of sea surface temperature gradients,” *Remote Sensing Letters.*, vol. 11, no. 12, pp. 1110–1117, 2020, doi: 10.1080/2150704X.2020.1825865.

[29] Chiba Prefecture, “Sanbaze Tidal Flat,” 1960. [Online]. Available: https://www.pref.chiba.lg.jp/kansei/sanbanze/keii/documents/201higata.pdf.

[30] “Zostera marina and tidal flat,” 2021. [Online]. Available: http://www.biodic.go.jp/moni1000/findings/reports/pdf/2020_amamoba_and_moba.pdf.

[31] “Case Study of Hakata Bay.” [Online]. Available: https://www.env.go.jp/water/博多湾の概要.pdf.

Appendices

Appendix 1 Main Workflow in Google Earth Engine (Modified Part)

```
Input the date range, interest region, Landsat number;
Calculate the coefficients;
Mosaic and export in batches.
```

```
// input basic model
Var
landsat=require('users/sofiaermida/landsat_smw_lst:modules/Landsat_LST.js')
var geometry = ee.Geometry.Polygon(
       [[[139.5730556,    35.70833333],
          [140.2788889,   35.72861111],
          [140.2705556,   34.84527778],
          [139.5591667,   34.85638889]]]);

Map.centerObject(geometry,8)

Map.addLayer(geometry,{},'studyarea')
var date_start = '';
var date_end = '';

var use_ndvi = true;

var LandsatColl = LandsatLST.collection('L8', date_start, date_end, geometry,
use_ndvi);
// print(LandsatColl);

// define the mosaicSameDate function
function mosaicByDate(imcol){
// convert the ImageCollection into List
var imlist = imcol.toList(imcol.size());
// print(imlist)

// Obtain the distinct image dates from the ImageCollection
var unique_dates = imlist.map(function(im){
    return ee.Image(im).date().format("YYYY-MM-dd");
  }).distinct();
// print(unique_dates);
```

```
// mosaic the images acquired on the same date
var mosaic_imlist = unique_dates.map(function(d){
    d = ee.Date(d);
    //print(d)
    var im = imcol.filterDate(d, d.advance(1, "day")).mosaic();
    //print(im)

// return the mosaiced same-date images and set the time properties
    return im.set(
      "system:time_start", d.millis(),
      "system:id", d.format("YYYY-MM-dd")
      );
  });
  return ee.ImageCollection(mosaic_imlist);
}

var LandsatColl_MosaicDate = mosaicByDate(LandsatColl).select("LST")
                                                       .map(function(img){
return    img.clip(roi).subtract(273.5).rename("SST").set("system:time_start",
img.date().millis());
                                                       });
print("LandsatColl_MosaicDate:",LandsatColl_MosaicDate);

var cmap1 = ['blue', 'cyan', 'green', 'yellow', 'red'];
var cmap2 = ['F2F2F2','EFC2B3','ECB176','E9BD3A','E6E600','63C600','00A600'];

// land cover masking
var dataset = ee.ImageCollection('JRC/GSW1_2/MonthlyRecurrence');

var visualization = {
  bands: ['monthly_recurrence'],
  min: 0.0,
  max: 100.0,
  palette: ['ffffff', 'ffbbbb', '0000ff']
};

// export after calculation
var imgSSTList = LandsatColl_MosaicDate.toList(LandsatColl_MosaicDate.size());
for(var i=0; i<imgSSTList.size().getInfo(); i++){
  var imgData = ee.Image(imgSSTList.get(i));
  var imgDate = imgData.date().format("YYYY-MM-dd").getInfo();
```

```
  Export.image.toDrive({
    image: imgData,
    description: 'SST-'+imgDate,
    scale: 30,
    region: roi,
    fileFormat: 'GeoTIFF',
    folder: 'JapanCoastSST',
    crs:"EPSG:32654"
  });

  // show the imageData
  Map.addLayer(imgData,{min:26, max:29, palette:cmap1}, 'SST-'+imgDate, false);
}  min: 0.0,
  max: 100.0,
  palette: ['ffffff', 'ffbbbb', '0000ff']
};
```

Appendix 2 Spatial Gradient Calculation

Calculate spatial gradient

```
// Load a Landsat 8 image and select the panchromatic band
var
image = ee.Image('LANDSAT/LC08/ ').select('');

// Compute the image gradient in the X and Y directions
var xyGrad = image.gradient();

// Compute the magnitude of the gradient
var gradient = xyGrad.select('x').pow(2)
          .add(xyGrad.select('y').pow(2)).sqrt();

// Compute the direction of the gradient
var direction = xyGrad.select('y').atan2(xyGrad.select('x'));

// Display the results
Map.setCenter(, , );
Map.addLayer(direction, {min: -2, max: 2, format: 'png'}, 'direction');
Map.addLayer(gradient, {min: -7, max: 7, format: 'png'}, 'gradient');
```

Acknowledgement

Upon the completion of this master thesis, I am really appreciated to those who have offered me great encouragement and support during the master course.

First, special acknowledgment is given to my respectable supervisor, professor Jun Sasaki whose patient instruction and constructive suggestions are beneficial to me a lot. Thanks to Prof. Sasaki that I understand what research and originality is and what changes I should make as a master's student compared to an undergraduate. Even after I leave school, this kind of thinking will benefit me for life.

Second, particular thanks are given to my co-supervisor, Prof. Satoh for his kind advice on how to make my master thesis more understandable and convincing.

What is more, I would like to present my thanks to all my colleagues. Without the support and help of these lovely colleagues, I am afraid I would not have been able to persevere until now, as I often feel lost.

Finally, I would like to extend my deep gratefulness to my family and friends, especially my two roommates, whose encouragement and support have made my accomplishments possible.